Microwave Dynamical Conductivity in the Quantum Hall Regime

Tomonori Arakawa,[1,*] Takashi Oka,[2] Seitaro Kon,[1] and Yasuhiro Niimi[3,4]

[1]National Institute of Advanced Industrial Science and Technology (AIST), National Metrology Institute of Japan (NMIJ), Tsukuba, Ibaraki 305-8563, Japan

[2]Institute for Solid State Physics, University of Tokyo, Kashiwa 277-8581, Japan

[3]Department of Physics, Graduate School of Science, Osaka University, Toyonaka, Osaka 560-0043, Japan

[4]Center for Spintronics Research Network (CSRN), Osaka University, Toyonaka, Osaka 560-8531, Japan

(Received 20 December 2021; accepted 10 June 2022; published 20 July 2022)

Dynamical conductivity contains information of dissipative and nondissipative processes induced by ac-electric fields. In the integer quantum Hall (QH) effect where the nondissipative Hall current is the most prominent feature, its robustness is assured by localized states within the Landau levels. We establish a noncontact method with a circular cavity resonator and detect the real and imaginary parts of the longitudinal and Hall conductivities at a microwave frequency in magnetic fields. The conventional Shubnikov–de Haas oscillations and QH plateaus are observed in the real parts of longitudinal and Hall conductivities, respectively, while periodic structures can be seen in the imaginary parts which are scaled by the QH filling factor. The latter originates from intra-Landau level transitions between different orbital angular momenta. The results demonstrate that the dynamical conductivity measurement provides microscopic information which is not accessible by conventional static methods. The present noncontact method would pave the way to reveal the electron dynamics in other two-dimensional systems such as twisted bilayer graphene.

DOI: 10.1103/PhysRevLett.129.046801

In quantum materials, various information of the electronic states can be obtained by applying an electric field and measuring the current, characterized by the longitudinal (σ_{xx}) and Hall (σ_{xy}) conductivities. For example, σ_{xx} informs us of insulator-metal transitions, while σ_{xy} indicates nondissipative Hall current which may originate from processes such as cyclotron motion in magnetic fields, or the Berry phase effect, etc. More detailed information can be obtained by studying the response of the current to the alternating electric field, where the conductivities are defined as complex values at a given frequency f, i.e., $\hat{\sigma}_{xx}(f) = \sigma'_{xx} + i\sigma''_{xx}$ and $\hat{\sigma}_{xy}(f) = \sigma'_{xy} + i\sigma''_{xy}$. By measuring both the real and imaginary parts of conductivities, we can evaluate the dissipative and nondissipative contributions at the same time. This enables us to approach the microscopic nature of quantum transport phenomena [1–5]. However, the experimental approach to such a "dynamical conductivity" measurement has not yet been established.

The integer quantum Hall (QH) effect [6] in a two-dimensional (2D) electron system is a prototypical quantum transport phenomenon which has a rich physical structure [7]. Despite its long history, little attention has been paid to the imaginary components which directly reflect the dynamic behavior. The real part of Hall conductivity σ'_{xy} in the QH regime has been addressed by the Faraday effect, where the polarization rotation of a linearly polarized electromagnetic wave is almost proportional to σ'_{xy} [8–14]. This approach allows investigating frequency evolution of the QH plateau [8,10,12,13,15–17]. Although Dziom *et al.* [13] have recently succeeded in estimating both σ'_{xy} and σ''_{xy} by evaluating the ellipticity of the transmitted wave in addition to the rotation angle, the origin of the imaginary component σ''_{xy} has not been elucidated. On the other hand, σ'_{xx} has been investigated in terms of the quantum phase transition between the QH plateaus [18–21]. For the imaginary component, Hohls *et al.* [20] found the nontrivial relation between σ'_{xx} and σ''_{xx} where a 2DEG with the Corbino geometry was connected to a coaxial line. Thus, the dynamical behavior of the QH effect has been *partially* addressed by using specialized methods where only one of the longitudinal or Hall conductivity has been discussed. However, to confirm the validity of the subtle imaginary components and to clarify the correspondence with the microscopic theory, it is essential to measure all the dynamical conductivity components simultaneously and compare them with a unified model.

In this Letter, we report the dynamical conductivities $\hat{\sigma}_{xx}$ and $\hat{\sigma}_{xy}$ of the 2D electron gas (2DEG) at a GaAs/AlGaAs heterojunction in the QH regime. By utilizing circular microwave modes (∼8.8 GHz) in a cavity resonator [22], we established a noncontact method to detect all the dynamical conductivities (σ'_{xx}, σ''_{xx}, σ'_{xy}, and σ''_{xy}). Systematic measurements as a function of magnetic field B and temperature T gave us the following results. The Shubnikov–de Haas oscillations and the QH plateaus were

detected in the real parts, σ'_{xx} and σ'_{xy}, respectively. Moreover, we observed periodic structures in the imaginary parts, σ''_{xx} and σ''_{xy}, which are scaled by the QH filling factor. We found that the observed circular dichroism in σ''_{xy} stems from the circular-dependent electron transition between the localized states with different orbital angular momenta. The present contactless method enables us to address the dynamical properties in a variety of 2D systems such as graphene [23], topological insulators [24], and layered materials [25–27].

The conventional methods using propagating electromagnetic waves require the careful calibration of the experimental system, because the microwave attenuation and phase shift depend on both the dissipative and nondissipative terms of the conductivities [28]. On the other hand, the cavity perturbation method with a resonance (standing) mode is widely used in condensed matter physics, where the dissipative (σ'_{xx} and σ''_{xy}) and nondissipative (σ'_{xy} and σ''_{xx}) terms are well separated into changes in the resonant frequency and full width at half maximum (FWHM), respectively. However, a conventional linearly polarized resonance mode yields only the longitudinal conductivities $\hat{\sigma}_{xx}$ [29,30]. Therefore, we have recently developed a method to independently measure two circularly polarized modes [22], which enables us to separate the diagonal and nondiagonal terms of the conductivity tensor.

In our experimental setup, a GaAs/AlGaAs wafer is placed in the cylindrical cavity and the 2DEG couples with the electric field of the right- (+) and left- (−) handed circularly resonant modes as shown in Fig. 1. The resulting modulation can be defined as $\Delta\hat{f}_{r\pm} = \Delta f_{r\pm} + i\Delta\Gamma_{\pm}/2 = (f_{r\pm} - f_0) + i(\Gamma_{\pm} - \Gamma_0)/2$, using complex resonance frequencies [31]. Here $f_{r\pm}$ and $\Gamma_{\pm}$ are the resonance frequencies and FWHMs, respectively, and f_0 and Γ_0 are the reference values without the 2DEG. As shown in Fig. 1, the incident microwave from port 1 (port 2) splits in half with a 90° relative phase difference at the coupler and selectively excites the left- (right-) handed circularly polarized mode. The reflected microwave at the cavity goes to another port. In other words, by measuring the transmission coefficients (S_{21} and S_{12}) we can independently detect $\Delta\hat{f}_{r+}$ and $\Delta\hat{f}_{r-}$, respectively.

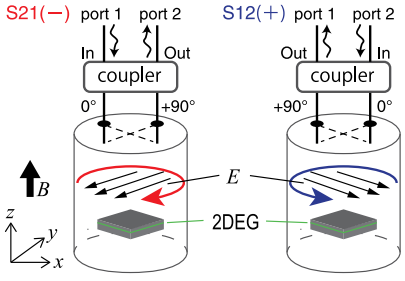

FIG. 1. Schematic image of the circularly polarized microwave interacting with the 2DEG. A rotating electric field (right- or left-handed circularly polarized microwave excited by S_{21} or S_{12}) couples to the 2DEG under a perpendicular magnetic field B.

Figure 2(a) shows our measurement system. All the measurements were performed at low temperatures ($T = 4.8$, 9.2, 18 K) using a cryostat and a perpendicular magnetic field B was applied to the 2DEG with a superconducting magnet. The frequency dependence of S_{21} and S_{12} was measured by a network analyzer. In Fig. 2(b), we show typical spectra measured at 4.8 K. Compared to the reference frequency f_0 without the 2DEG conductivity (vertical dashed line), the resonance frequencies $f_{r\pm}$ are shifted due to the interaction with the 2DEG via the rotating electric field. Based on the microwave cavity perturbation technique [30,31], the relations between the shift in the resonance ($\Delta f_{r\pm}$ and $\Delta\Gamma_{\pm}/2$) and the dynamical conductivity of the 2DEG are obtained as

$$\Delta f_{r\pm} = \gamma(\pm\sigma'_{xy} - \sigma''_{xx}), \tag{1}$$

$$\Delta\Gamma_{\pm}/2 = \gamma(\sigma'_{xx} \pm \sigma''_{xy}), \tag{2}$$

where γ is the coupling constant [32]. Note that in the conventional method with a linearly polarized resonance

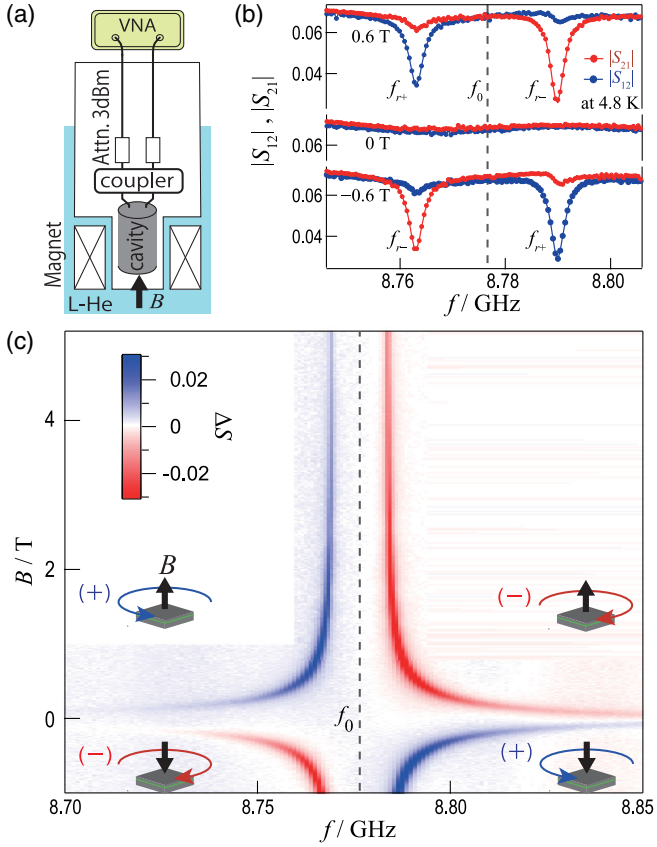

FIG. 2. (a) Schematic image of our measurement system. (b) Transmission coefficients (S_{21} and S_{12}) measured at 4.8 K for $B = 0$, ±0.6 T. (c) Color plot of ΔS as a function of f and B measured at 4.8 K.

mode, only $\hat{\sigma}_{xx}$ affects the resonance mode, and the $\hat{\sigma}_{xy}$ component is not detectable. According to Eq. (1), the frequency shift $\Delta f_{r\pm}$ depends on the polarization of the resonant mode as well as the value of σ'_{xy}, which is an odd function of B. As shown in Fig. 2(b), the measured S_{21} and S_{12} at $B = \pm 0.6$ T clearly show this tendency: As σ'_{xy} is negative in an electron system, the resonant peak in S_{21} (S_{12}) shifts to the positive (negative) side with respect to f_0 for $B = 0.6$ T. In addition, the measured S_{21} and S_{12} show only one of the circular resonant peaks, indicating that the polarization selective detection successfully works. At $B = 0$ T, $f_{r+} = f_{r-}$ is expected from Eqs. (1) and (2), and this was confirmed at room temperature [32]. However, at low temperatures, the resonance peaks disappear at around $B = 0$ T due to the broadening of the peaks as σ'_{xx} increased [see Fig. 2(b)].

To see the magnetic field dependence more clearly, we define the difference of the transmission coefficients as $\Delta S \equiv |S_{21}| - |S_{12}|$. Figure 2(c) shows a color plot of ΔS obtained at $T = 4.8$ K as a function of B and f. The blue and red regions correspond to the right- and left-handed circular resonant peaks, respectively. The clear symmetric pattern with respect to f_0 and $B = 0$ directly reflects the Onsager reciprocal relations. $|\Delta f_+|$ and $|\Delta f_-|$ gradually decrease with increasing B and are saturated to finite values. The origin of the symmetric pattern is discussed in detail in the next paragraph, while the saturation is related to the small breaking of the 4th rotational symmetry of the cylindrical cavity in the x-y plane. Considering the symmetry breaking factor δ, we modified Eqs. (1) and (2) and obtain all the dynamical conductivity components (σ'_{xx}, σ''_{xx}, σ'_{xy}, and σ''_{xy}) as follows:

$$\sigma'_{xy} = \frac{f_{r+} - f_{r-}}{2\gamma}\sqrt{1 - \gamma^2\left(\frac{2\omega_0\delta}{f_{r+} - f_{r-}}\right)^2}, \tag{3}$$

$$\sigma'_{xx} = \frac{\Gamma_+ + \Gamma_- - 2\Gamma_0}{4\gamma}, \tag{4}$$

$$\sigma''_{xy} = \frac{\Gamma_+ - \Gamma_-}{4\gamma} \Big/ \sqrt{1 - \gamma^2\left(\frac{2\omega_0\delta}{f_{r+} - f_{r-}}\right)^2}, \tag{5}$$

$$\sigma''_{xx} = -\frac{f_{r+} + f_{r-} - 2f_0}{2\gamma}. \tag{6}$$

Four values ($f_{r\pm}$ and $\Gamma_\pm$) are experimentally obtained by fitting the measured S_{21} and S_{12} with the Lorentz function. Two unknown parameters δ and γ are estimated by using Eq. (3) and the quantized values at two QH plateaus, while Γ_0 and f_0 are determined at the maximum magnetic field ($B = 5.2$ T) [32].

Figures 3(a) and 3(b) show the real (σ'_{xy} and σ'_{xx}) and imaginary components (σ''_{xy} and σ''_{xx}) of the obtained dynamical conductivities, respectively. The insets show

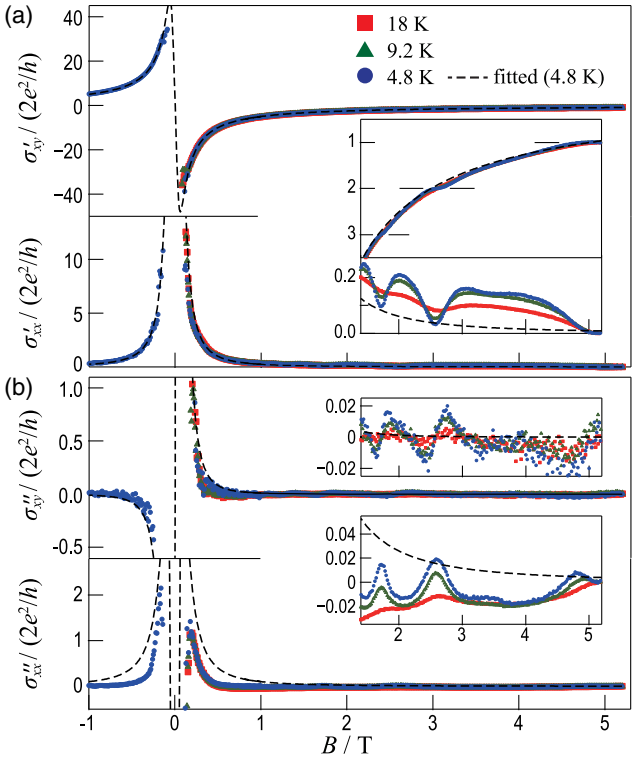

FIG. 3. (a) Real and (b) imaginary components of the dynamical conductivity as a function of B measured at three different temperatures ($T = 4.8$, 9.2, and 18 K). The dashed lines are the best fits with Eqs. (5)–(7) for $T = 4.8$ K. The insets in (a) and (b) show the magnified views of the high magnetic field region.

the magnified data in the high B region. We first discuss the full-scale data using a classical picture. According to the Drude model, the high-frequency conductivities under B are given by

$$\hat{\sigma}_{xx} = \sigma_0\left[\frac{1 + 2\pi i f\tau}{1 + 4\pi^2(f_c^2 - f^2)\tau^2 + 4\pi i f\tau}\right], \tag{7}$$

$$\hat{\sigma}_{xy} = -\sigma_0\left[\frac{2\pi f_c\tau}{1 + 4\pi^2(f_c^2 - f^2)\tau^2 + 4\pi i f\tau}\right], \tag{8}$$

$$\sigma_0 = n_e e^2\tau/m_e. \tag{9}$$

Here $f_c = eB/2\pi m_e$ is the cyclotron frequency, m_e is the effective mass, n_e is the electron density, and τ is the relaxation time. The experimental curves in Figs. 3(a) and 3(b) are fitted by Eqs. (7)–(9) with $m_e = 0.067m_0$ [35] in the magnetic field range of $0.2 < B < 1$ T. In this range, the linearity of our perturbation method is well ensured because of the low conductivities [32]. Note that four curves (σ'_{xy}, σ'_{xx}, σ''_{xy}, and σ''_{xx}) at each temperature were fitted with two fitting parameters (n_e and τ) in a consistent manner. The fitted result at $T = 4.8$ K is shown in Fig. 3. The overall shapes are nicely reproduced and the obtained values ($n_e \sim 2.46 \times 10^{11}$ cm^{-2} and

$\tau \sim 7.5$ ps) are quantitatively consistent with those estimated from conventional static measurement at 77 K ($n_e \sim 2.3 \times 10^{11}$ cm^{-2} and $\tau \sim 4.6$ ps).

Now we move to the high B region where the classical picture breaks down and enters the QH regime. In the inset of Fig. 3(a), we show the real parts of the dynamical conductivity above 1 T. With increasing B, the QH plateau in σ'_{xy} and the Shubnikov–de Haas oscillation in σ'_{xx} become clearer. To see this behavior more quantitatively, the obtained dynamical conductivities shown in Figs. 3(a) and 3(b) are plotted as a function of the filling factor $\nu = n_e h/eB$ in Figs. 4(a) and 4(b). Here, $n_e = 2.49 \times 10^{11}$ cm^{-2} was estimated from the period of the Shubnikov–de Haas oscillation, which is in good agreement with the value obtained from the Drude model fitting. The obtained QH plateaus and the Shubnikov–de Haas oscillation are nicely scaled by ν, and the QH plateaus are quantitated to $e^2/h \times \nu$ [see the inset of Fig. 4(a)]. These are typical behaviors of the QH effect [8,19,20,36]. We also observed periodic structures in the imaginary components (σ''_{xy} and σ''_{xx}) as shown in Fig. 4(b). These structures are enhanced with decreasing T and nicely scaled by ν, indicating that they originate from the QH effect.

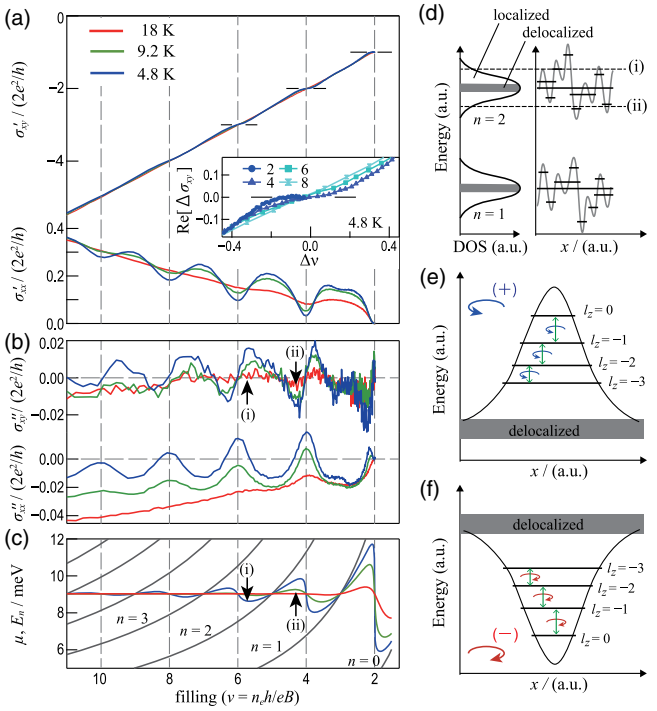

FIG. 4. (a) Real and (b) imaginary components of the dynamical conductivity as a function of ν at three different temperatures ($T = 4.8$, 9.2, and 18 K). The inset in (a) shows the comparison of the QH plateaus with different filling factors. (c) Chemical potential μ and Landau level energies calculated with experimental condition ($T = 4.8$, 9.2, 18 K, $m_e = 0.067 m_0$, and $n_e = 2.49 \times 10^{11}$ cm^{-2}). (d) Schematics of the energy levels of the QH state as a function of density of states (DOS) and position. (e),(f) Schematic energy diagram of the eigenenergy and the possible transitions between the localized states in the presence of a potential hill (e) and potential valley (f), respectively.

Although the similar periodic behavior in σ''_{xy} was observed by Dziom *et al.* [13] at 134 and 202 GHz, its origin has not been fully elucidated. In addition, σ''_{xy} was accompanied by a parabolic background, which hinders the quantitative analyses such as the precise amplitude and period. In the present case, σ''_{xy} always crosses zero at the integer filling accompanied by a sign reversal. It should be noted that such an oscillatory behavior of σ''_{xy} with a sign change was realized owing to our original perturbation method with a circular cavity. Physically, $\sigma''_{xy} \propto \Gamma_+ - \Gamma_-$ reflects the circular dichroism of the dissipative process: in other words, $\sigma''_{xy} > 0$ (or $\sigma''_{xy} < 0$) implies that the dissipation process, i.e., electron-hole pair excitation induced by microwaves, is predominant for left-handed (or right-handed) circular polarization. Furthermore, we succeeded in observing a clear temperature dependence of σ''_{xy} as shown in Fig. 4(b). Figure 4(c) shows the calculated chemical potential μ and Landau level (LL) energies E_n as a function of ν at each temperature, where n is the quantum number [32]. As detailed in the next paragraph, there is a clear correlation between σ''_{xy} and μ with respect to ν and temperature.

We now discuss the origin of the oscillation in σ''_{xy} in terms of the *intra*-Landau level structure [32]. It is well established that the *inter*-Landau level transition between the LLs exhibit a circular dichroism: the transition from nth LL to $n+1$th LL is possible only with (+) polarization [37]. In fact, σ''_{xy} near $B \approx 0$ [see Fig. 3(b)] reflects the increased dissipation related to this transition. On the other hand, for small n regions where the QH plateau is visible, the energy between two adjacent LLs is much larger than that of the microwave. Thus, we need to consider the fine structure within each LLs to explain the present experimental results. When plotted against the filling ν, σ''_{xy} shows a nontrivial oscillation with a weak jumplike behavior [see Fig. 4(b)]. Interestingly, this behavior resembles that of the chemical potential μ with an overall sign difference [see Fig. 4(c)]: in other words, σ''_{xy} is positive or negative when μ is located at the upper or lower sides of LLs, respectively. This suggests that the chirality of the microwave absorption changes sign at the center of the LLs and jumps when transferring to different LLs. In realistic 2DEGs, the LLs are broadened by disorder as illustrated in Fig. 4(d) [38–40]. The center of the broadened LL is dictated by extended states, while the low and high energy ends are described by localized states. There is a qualitative difference between the low and high energy localized states. A simplified model that describes this was given by Yoshioka [41] where a single isotropic impurity potential with positive [(e) "hill"] or negative [(f) "valley"] signs was introduced [see Figs. 4(e) and 4(f)]. Because of the approximate isotropy, the orbital angular momentum $\hbar l_z$ of

the Landau states is also a good quantum number of the localized states. However, its correlation with energy is opposite, i.e., $\hbar l_z$ increases (decreases) with energy for the upper (i) [lower (ii)] ends of the LL, respectively. Assuming the electric dipole transition, we obtain the following selection rule: for upper LL states, the transition from l_z to $l_z + 1$ is realized only with (+) polarization, whereas for lower LL states, the transition from l_z to $l_z - 1$ is realized only with (−) polarization [see Figs. 4(e) and 4(f)]. Because the relative proportion of hills and valleys changes with μ, an imbalance in the circular dependent transitions occurs. Therefore, we conclude that the circular dichroism in σ''_{xy} originates from the transition between two adjacent localized states (i.e., $l_z \rightarrow l_z \pm 1$) within the same LL. Our result directly reflects the unique dynamics of localized electrons, i.e., rotational motion characterized by orbital angular momentum l_z in the same Landau index, which has never been detected so far.

Finally, let us mention another imaginary part σ''_{xx}. From the phenomenological viewpoint, capacitive and inductive components in the system can contribute to positive and negative shifts in σ''_{xx}. This tendency is qualitatively consistent with the data in Fig. 4(b): the localized electrons are frozen (capacitive) at the integer filling, and they can transport (inductive) at around the half-integer filling. A further study is desirable to clarify the microscopic picture of the observed σ''_{xx}.

In conclusion, we succeeded in measuring all the dynamical conductivities of a 2DEG by using the contactless method with a circular cavity resonator, and the dynamical behavior in the QH regime was investigated. In addition to the conventional behavior (the Shubnikov–de Haas oscillations and the QH plateaus), we detected periodic structures in the imaginary parts of the dynamical conductivities, σ''_{xx} and σ''_{xy}. Based on a simple model, we conclude that the obtained circular dichroism in σ''_{xy} originates from the circular dependent electron transition between two adjacent orbital angular momenta states within the same LL index. Such a dynamical feature of localized electrons is revealed for the first time. In addition, our method allows the direct evaluation of circular conductivities $\hat{\sigma}_{\pm} \equiv \pm\hat{\sigma}_{xy} + i\hat{\sigma}_{xx}$, which is often used in theory. The achievements demonstrated in this work will stimulate efforts towards deeper understandings of various quantum transport phenomena in various 2D electron systems such as the anomalous QH effect [24] and superconductivity [25,27].

We thank K. Asano, M. Koshino, S. Yamada, S. Hidaka, M. Ferrier, T. Hata, S. Norimoto, and S. Iwakiri for valuable discussions. We appreciate the 2DEG wafer from K. Kobayashi. This work was supported by JSPS KAKENHI Grants No. JP18H01815, No. JP22H01964, No. JP16H05964, and No. JP22H01936; JST CREST Grant No. JPMJCR19T3, and JST ERATO-FS Grant No. JPMJER2105, Japan.

*Corresponding author.
tomonori-arakawa@aist.go.jp

[1] O. S. Barišić, J. Kokalj, I. Balog, and P. Prelovšek, Phys. Rev. B **94**, 045126 (2016).
[2] M. Swanson, Y. L. Loh, M. Randeria, and N. Trivedi, Phys. Rev. X **4**, 021007 (2014).
[3] C. J. Tabert and E. J. Nicol, Phys. Rev. B **86**, 075439 (2012).
[4] A. D. Maestro, B. Rosenow, J. A. Hoyos, and T. Vojta, Phys. Rev. Lett. **105**, 145702 (2010).
[5] C. S. Ting, S. C. Ying, and J. J. Quinn, Phys. Rev. B **14**, 4439 (1976).
[6] K. v Klitzing, G. Dorda, and M. Pepper, Phys. Rev. Lett. **45**, 494 (1980).
[7] R. E. Prange, M. E. Cage, K. Klitzing, S. M. Girvin, A. M. Chang, F. Duncan, M. Haldane, R. B. Laughlin, A. M. M. Pruisken, and D. J. Thouless, *The Quantum Hall Effect* (Springer, New York, 2012).
[8] F. Kuchar, R. Meisels, G. Weimann, and W. Schlapp, Phys. Rev. B **33**, 2965 (1986).
[9] I. Crassee, J. Levallois, A. L. Walter, M. Ostler, A. Bostwick, E. Rotenberg, T. Seyller, D. van der Marel, and A. B. Kuzmenko, Nat. Phys. **7**, 48 (2011).
[10] Y. Ikebe, T. Morimoto, R. Masutomi, T. Okamoto, H. Aoki, and R. Shimano, Phys. Rev. Lett. **104**, 256802 (2010).
[11] R. Shimano, G. Yumoto, J. Y. Yoo, R. Matsunaga, S. Tanabe, H. Hibino, T. Morimoto, and H. Aoki, Nat. Commun. **4**, 1841 (2013).
[12] A. V. Stier, C. T. Ellis, J. Kwon, H. Xing, H. Zhang, D. Eason, G. Strasser, T. Morimoto, H. Aoki, H. Zeng, B. D. McCombe, and J. Cerne, Phys. Rev. Lett. **115**, 247401 (2015).
[13] V. Dziom, A. Shuvaev, A. V. Shchepetilnikov, D. MacFarland, G. Strasser, and A. Pimenov, Phys. Rev. B **99**, 045305 (2019).
[14] V. Suresh, E. Pinsolle, C. Lupien, T. J. Martz-Oberlander, M. P. Lilly, J. L. Reno, G. Gervais, T. Szkopek, and B. Reulet, Phys. Rev. B **102**, 085302 (2020).
[15] T. Morimoto, Y. Hatsugai, and H. Aoki, Phys. Rev. Lett. **103**, 116803 (2009).
[16] T. Morimoto, Y. Avishai, and H. Aoki, Phys. Rev. B **82**, 081404(R) (2010).
[17] Z. Gevorkian, V. Farztdinov, and Y. Lozovik, Physica (Amsterdam) **111E**, 148 (2019).
[18] A. L. Efros, Sov. Phys. JETP **62**, 1057 (1985), https://ui.adsabs.harvard.edu/abs/1985JETP...62.1057E/abstract.
[19] L. W. Engel, D. Shahar, C. Kurdak, and D. C. Tsui, Phys. Rev. Lett. **71**, 2638 (1993).
[20] F. Hohls, U. Zeitler, and R. J. Haug, Phys. Rev. Lett. **86**, 5124 (2001).
[21] F. Hohls, U. Zeitler, R. J. Haug, R. Meisels, K. Dybko, and F. Kuchar, Phys. Rev. Lett. **89**, 276801 (2002).
[22] T. Arakawa, S. Norimoto, S. Iwakiri, T. Asano, and Y. Niimi, Rev. Sci. Instrum. **90**, 084707 (2019).
[23] K. S. Novoselov, A. K. Geim, S. V. Morozov, D. Jiang, Y. Zhang, S. V. Dubonos, I. V. Grigorieva, and A. A. Firsov, Science **306**, 666 (2004).
[24] J. G. Checkelsky, R. Yoshimi, A. Tsukazaki, K. S. Takahashi, Y. Kozuka, J. Falson, M. Kawasaki, and Y. Tokura, Nat. Phys. **10**, 731 (2014).

[25] M. Yankowitz, S. Chen, H. Polshyn, Y. Zhang, K. Watanabe, T. Taniguchi, D. Graf, A. F. Young, and C. R. Dean, Science **363**, 1059 (2019).
[26] T. Sekihara, R. Masutomi, and T. Okamoto, Phys. Rev. Lett. **111**, 057005 (2013).
[27] N. Reyren, S. Thiel, A. D. Caviglia, L. F. Kourkoutis, G. Hammerl, C. Richter, C. W. Schneider, T. Kopp, A.-S. Rüetschi, D. Jaccard, M. Gabay, D. A. Muller, J.-M. Triscone, and J. Mannhart, Science **317**, 1196 (2007).
[28] R. F. O'Connell and G. Wallace, Phys. Rev. B **26**, 2231 (1982).
[29] V. Krasovitsky, D. Terasawa, K. Nakada, S. Kozumi, A. Sawada, and N. Sato, Cryogenics **44**, 183 (2004).
[30] O. Klein, S. Donovan, M. Dressel, and G. Grüner, Int. J. Infrared Millim. Waves **14**, 2423 (1993).
[31] J. O. Artman and P. E. Tannenwald, J. Appl. Phys. **26**, 1124 (1955).
[32] See Supplemental Material at http://link.aps.org/supplemental/10.1103/PhysRevLett.129.046801 for experimental details and theoretical description, which includes Refs. [33,34].
[33] D. M. Pozar, *Microwave Engineering*, 4th ed. (Wiley, Hoboken, NJ, 2012).
[34] C. H. Papas, J. Appl. Phys. **25**, 1552 (1954).
[35] S. M. Sze and K. K. Ng, *Physics of Semiconductor Devices* (Wiley, New York, 2006).
[36] P. J. Burke, I. B. Spielman, J. P. Eisenstein, L. N. Pfeiffer, and K. W. West, Appl. Phys. Lett. **76**, 745 (2000).
[37] I. O. Nedoliuk, S. Hu, A. K. Geim, and A. B. Kuzmenko, Nat. Nanotechnol. **14**, 756 (2019).
[38] K. Hashimoto, C. Sohrmann, J. Wiebe, T. Inaoka, F. Meier, Y. Hirayama, R. Römer, R. Wiesendanger, and M. Morgenstern, Phys. Rev. Lett. **101**, 256802 (2008).
[39] Y. Niimi, H. Kambara, T. Matsui, D. Yoshioka, and Hiroshi Fukuyama, Phys. Rev. Lett. **97**, 236804 (2006).
[40] S. Ilani, J. Martin, E. Teitelbaum, J. H. Smet, D. Mahalu, V. Umansky, and A. Yacoby, Nature (London) **427**, 328 (2004).
[41] D. Yoshioka, J. Phys. Soc. Jpn. **76**, 024718 (2007).